Journal of Solid and Fluid Mechanics (JSFM), 14(5): 1-5, 2025

Shahrood University of Technology

Journal of Solid and Fluid Mechanics (JSFM)

DOI: 10.22044/jsfm.2025.15285.3913

Manufacturing Engineering of Iran

# Numerical Study of Advance Ratio Effect on Dynamic Stall of the Helicopter Rotor Blade in Forward Flight

**Farid Hosseinzadeh Esfahani [1, *], S.M.H Karimian [2]**

[1] Ph.D. researcher, Department of Aerospace Engineering, Amirkabir University of Technology, Tehran, Iran
Prof., Department of Aerospace Engineering, Amirkabir University of Technology, Tehran, Iran

*Corresponding author: f.hosseinzadeh@aut.ac.ir

Received: 2024/29/10 Revised: 2024/17/11 Accepted: 2025/04/01

## Abstract

In this study, numerical simulations are used to investigate the dynamic stall phenomenon at two advance ratios: $\mu$ = 0.3 and $\mu$= 0.35, on a single blade with cyclic pitching motion. To simulate the three-dimensional compressible flow field, the Unsteady Reynolds-averaged Navier-Stokes (URANS) equations are solved using the finite volume discretization method. A hybrid mesh is employed, and turbulence is modeled using the k-$\omega$ SST model. To validate and verify the numerical method, flight test data from the AH-1G helicopter was used. The comparison results confirm the accuracy and reliability of the numerical approach applied in this study. The findings of this study indicate that contrary to expectations, the intensity and number of stalls on the retreating side of the rotor at the studied radial section ($r/R$ = 0.778) are greater at $\mu$ = 0.3 compared to $\mu$ = 0.35. On the advancing side, the stall is more severe at $\mu$ = 0.35, with the post-stall pitching moment coefficient differing by 89%, resulting in a significant increase in negative aerodynamic damping at this advance ratio. An analysis of the flow pattern reveals that the dynamic stall development at both advance ratios begins with flow separation near the trailing edge, which then propagates upstream while simultaneously bend to outboard region due to radial flow.

**Keywords:** Numerical simulation; Dynamic stall; Helicopter Rotor; Advance Ratio; Aerodynamic Damping

## 1. Introduction

The phenomenon of unsteady separation and dynamic stall in helicopter rotor blades occurs at specific forward flight speeds or during severe maneuvers when the blade pitch angle exceeds the static stall angle of attack. This phenomenon is considered one of the most complex flow phenomena in helicopter and wind turbine rotor aerodynamics. The formation of dynamic stall vortex (DSV) causes severe changes in aerodynamic forces and moments, the undesirable effects of which include excessive vibrations and even the creation of additional rolling moments around the center of rotation of the helicopter rotor. In fact, this phenomenon is considered the cause of the limitations of forward speed and extreme maneuvers in the flight envelope of helicopters. Numerous experimental studies [1-4] have been conducted on oscillating airfoil to identify the mechanism of dynamic stall formation and the parameters affecting it, including the effect of airfoil type, oscillation amplitude, oscillation rate, reduced frequency, and compressibility on aerodynamic coefficients. These studies have provided valuable information to researchers in this field. Since the late 1990s, when computational fluid dynamics (CFD) developed, extensive numerical simulations of oscillating airfoil dynamic stall were performed and compared with previous experimental studies, which caused more insight about dynamic stall details [5,6].

However, the aerodynamic environment of helicopter rotors has unique three-dimensional features that were not visible in this type of research. Researchers in this field then studied the pitching wing to better understand three-dimensional flow conditions in the rotor. for instance, Coton and Galbraith [7] studied the dynamic stall in a pitching finite wing n wind tunnel. According to the findings of this study, that the dynamic stall began at the mid-span of the wing, and as the DSV fully formed, its maximum strength developed at the mid-span. Le Pape et al. [8] utilized laser Doppler velocimetry (LDV) and particle imaging velocimetry (PIV) techniques in a wind tunnel to investigate the dynamic stall and chaotic nature of the flow separated from the pitching wing. Their study was specifically aimed at investigating the three-dimensional effects on dynamic stall behavior. Their observations showed that DSV extended from the inner region to the outer regions, which were limited by the tip vortex. They also found that the wing sweep angle could have a significant effect on the dynamic stall. Numerical simulation has helped researchers study spanwise flow

on a pitching finite wing and tip vortex. Spentzos et al. [9, 10] examined flow topology during dynamic stall with limited computational resources, a major development in this field. Their results showed that the interaction of the blade tip vortex and the dynamic stall vortex caused the formation of an omega vortex had good qualitative consistency with earlier flow studies in experimental results. authors also noted that despite the investigation of different wing tip shapes, the changes in the flow patterns in the wing tip region are small. With the increase in computing power in the mid-2000s, it motivated researchers to investigate stall dynamics in the rotating environment. Letzgus et al. [11] studied the Airbus H-145 helicopter's rotor dynamic stall during high-speed turning flight numerically. The study's findings revealed that during this maneuver, a complex flow field formed around the rotor blade, which experienced extensive flow separations, multiple dynamic stalls, streamwise vortices, and shock-induced separation. Also, their findings showed that the separation initiated at the trailing edge and spread toward the leading edge. Hosseinzadeh and Karimian [12] conducted numerical simulations to study the rotor blade's dynamic stall at two forward flight speeds. They found that during blade pitch-up motion, a large and stretched vortex, similar to a swell structure, formed in the third quadrant of the rotor disk and gradually diminished and disappeared as the blade approached the fourth quadrant. They also found that radial flow was prominent in the fourth quadrant of rotor blade rotation, resulting in significant changes in the vorticity field in this region.The aim of this research is to numerically simulate and investigate the complex flow field around a helicopter rotor blade at two advance ratios in forward flight of the helicopter. This analysis focuses on justifying the aerodynamic coefficients and providing details of the dynamic stall cycle and the formation of various vortices at a significant radial section of the blade (*r/R*=0.778).

## 2. Case study

Figure 1 illustrates the geometry of the blade under investigation in this study. The blade has a radius of 5.5 meters from the center of rotation and two profiles along its span. In this planform, a NACA23012 airfoil is employed from the center of rotation for the first 4.279 meters of the blade (including the hinge offset), or up to *r/R*=0.778. The NACA13008 airfoil is then employed between the radial locations of the blade, which ranges from 5.225 to 5.5 m, or from *r/R* = 0.85 to the tip. During the transition zone from *r/R*=0.778 to *r/R*=0.85, the airfoil smoothly transitions from NACA23012 to NACA13008. The airfoils used from the beginning of the blade to the tip start area at *r/R*=0.95 have a constant chord of 0.35 m. The airfoils employed from the blade's commencement until the tip start area at *r/R*=0.95 have a constant chord of 0.35 meters. This blade has a 13.95 aspect ratio and no geometric twist; the blade tip is also parabolic. The blade is initially located on the hypothetical helicopter's tail at azimuth angle of $\psi$ = 0 degrees, and it rotate counterclockwise, as seen in Western designs.

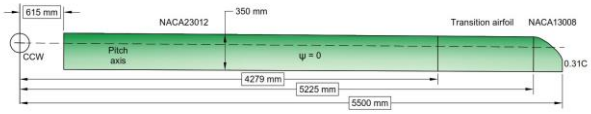


**Figure 1. Rotor blade planform**

The change in blade pitch angle with azimuth angle is applied to the blade using the following equation [13].

$$\theta = \theta_o + \theta_{1c} \cos\psi(t) + \theta_{1s} \sin\psi(t) \qquad (1)$$

The control angles are determined based on the helicopter's stability characteristics at different flight speeds. The blade control pitch angles for the two advance ratios studied are mentioned in Table1.

**Table 1. Flight conditions and control pitch angles**

| Flight No | $\mu$ | $M_\infty$ | $\theta_0$ | $\theta_{1C}$ | $\theta_{1S}$ |
|---|---|---|---|---|---|
| 1 | 0.35 | 0.232 | 13.89º | 1.34º | -5.7º |
| 2 | 0.3 | 0.196 | 11.95º | 0.89º | -3.81º |

Also, the rotational speed is 40.3 rad/sec at both flight speeds.

## 3. Methodology

### 3.1. Numerical Domain

The computational domain in this study consists of three domains. First, a cylindrical capsule-shaped domain is created around the blade. The cyclic pitching motion of the rotor blade is controlled by the dynamic rigid motion in this region. Based on equation (1), the sliding mesh technique is utilized to apply pitching motion to this region. The second domain is a cylindrical zone that includes the first domain. The rotation of the rotor blade defines this domain, which slides over the boundary interface with the third domain. The third domain is the outer domain, which is a stationary sphere defined to simulate the effect of the far field. The no-slip boundary conditions on the rotor blade and the pressure far-field are applied to the outer domain. The three domains, including the pitching, rotational, and stationary, are connected by four interface boundary conditions.

### 3.2. Mesh generation

The multi-zone approach is used to generate a hybrid mesh in the first domain, which consists of a structured mesh of hexahedrons in the boundary layer and a tetrahedral unstructured mesh outside of it. The boundary layer mesh on the blade surface is generated with a height of the first cell from the surface is $2.81\times10^{-6}$ m, and the growth ratio

is 1.1 for 26 boundary layers. Considering the above conditions, the average value of $y+$ during a complete rotation of the rotor blade is always less than one. The mesh in the rotating cylinder region and the outer spherical region is of the tetrahedral unstructured meshes. For the selected appropriate meshes ($\mu$ = 0.35), three meshes with 3.17, 9.1, and 14.1 million cells were investigated. The difference in the average lift coefficient of the second mesh compared to the first was 3.8%, and compared to the third mesh, it was 1.2%, which is considered a small variation for this flow configuration.

### 3.3. Governing equation and numerical solution

In this study, the three-dimensional compressible turbulent flow around an isolated helicopter rotor blade is numerically solved using the unsteady Reynolds averaged Navier-Stokes (URANS) equations using the finite volume discretization approach. Equation (2) presents the integral form of the governing equations used.

$$\frac{\partial}{\partial t}\int_{\Omega}\overrightarrow{W}\,d\Omega+\oint_{\partial\Omega}(\overrightarrow{F_C}-\overrightarrow{F_V})\,ds=0 \qquad (2)$$

In the aforementioned equation, W represents the vector of variables, $F_C$ denotes the convective fluxes vector, and $F_V$ represents the viscous fluxes vector. The second-order Roe-FDS upwind scheme [14] has been employed for the discretization of the convective fluxes [15]. For better accuracy, a second-order implicit time discretization scheme with a dual-time formulation [16] has been used to separate time periods. For turbulence modeling, the shear stress transport $k$-$\omega$ SST model has been adopted. This model provides reliable accuracy for predicting the onset and location of flow separation under strong adverse pressure gradients [16]. The time step size was selected as $1.82\times10^{-4}$ sec (1440 time steps) to accurately capture the time-varying characteristics of the complex flow field in the dynamic stall.

### 3.4. Validation and verification

The numerical method used in this study is confirmed by comparing the normal force coefficient on two radial sections of the rotor blade of the AH1-G helicopter. Flight test results at maximum flight speed of 290 km/h ($\mu$ = 0.37) were utilized to determine the normal force coefficient in radial sections at $r/R$ = 0.86 and $r/R$ = 0.95. As shown in Figure 2, the current results at the section $r/R$ = 0.86, except for limited azimuth angles, are in excellent agreement with the flight test results at other azimuth angles. The maximum error between the vertical force coefficient of the present study and the flight data that occurred at the azimuth angle of $\psi$ = 270 degrees is 12%. Furthermore, when comparing the current results to the results of the FLOWer solver, it is clear that the simulation's accuracy in predicting the location of the maximum coefficient and its quantitative value is better than the results of this solver presented in reference [17]. This also applies to the section $r/R$ = 0.95. In this radial region, comparing the simulation results to the flight test results reveals that, while the normal force behavior is similar, it loses its quantitative match. However, the modeling of the normal force coefficient in this section is more accurate than the FLOWer solver. The maximum error occurred at $\psi$ = 275 degrees, and it was 14% at this section of the blade.

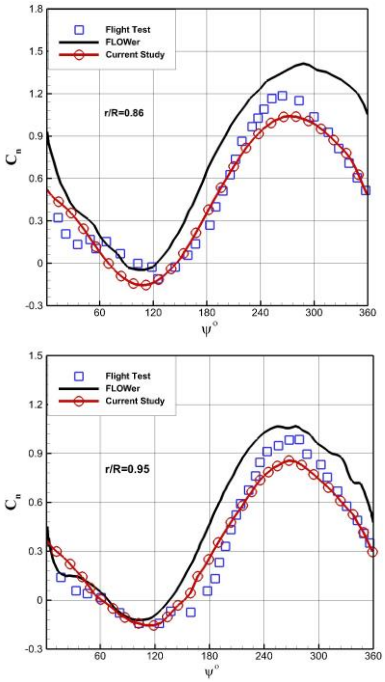


**Figure 2. Comparison of present results with experimental data and numerical results [17] at (Up) r/R = 0.86 and (Down) r/R = 0.95.**

## 4. Results and Discussion

The aerodynamic loads in the studied radial section have been calculated at two advance ratios of 0.3 and 0.35 according to the flight conditions of Table 1 and are shown in Figure 3. The method of analyzing aerodynamic loads in this section is to consider sudden changes in the pitching moment and lift coefficients as a local dynamic stall in the radial section, provided that they confirm each other within an acceptable azimuth angle range. The pre-stall lift coefficient increased linearly at both advance ratios as rotation began. In the first quadrant, the rotor blade pitch angle decreased, but the section's tangential speed increased continuously. In this region, stall occurs in advance ratio 0.35 earlier and at higher pitch angle than in advance ratio 0.3. Furthermore, the loss in lift coefficient is most evident in advance ratio 0.35. The first stall at both advance ratios is associated with the formation of shock waves near the airfoil's leading edge. Similar to the lift coefficient, the pitching moment coefficient has a severe stall at both advance ratios. This stall is also due to the

increase in tangential velocity at the leading edge and the creation of a shock wave. The existence of a shock wave near the leading edge increases local pressure near the leading edge of the airfoil, causing the pitching moment coefficient to stall in the first quadrant of flight [18]. Due to the high sensitivity of the pitching moment coefficient to the shock wave pressure gradient near the leading edge, this phenomenon increases the stall time difference between the pitching moment and lift coefficients in this region of the rotor blade movement. The maximum difference between the two advance ratios in the nose-down pitching moment coefficient in the post-stall region is about 89%. This can have a significant effect on the average aerodynamic damping, causing severe radial section fluctuations at $\mu$ = 0.35 [18].

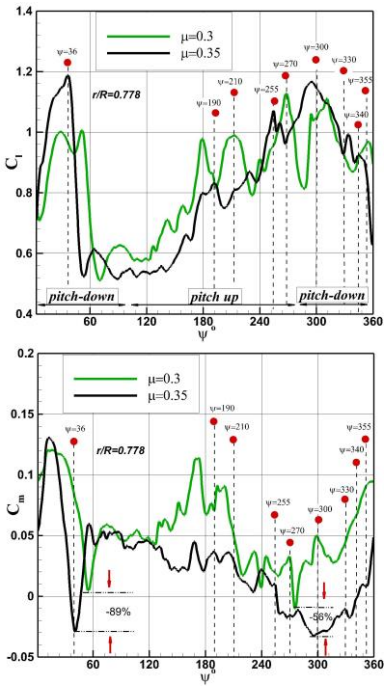


**Figure 3. Time history of lift coefficient (Up) and pitching moment coefficient (Down) of the studied section (r/R = 0.778)**

As the rotor blade enters the retreating side, the lift coefficient experiences several dynamic stalls at both flight speeds, most of which occur at advance ratio of 0.3. At this advance ratio, three substantial stalls occur at angles $\psi$ = 180°, $\psi$ = 210°, and $\psi$ = 270°, as confirmed by the pitching moment coefficient. Despite expectations of stall conditions at high-flying speeds, we only see one substantial stall at $\psi$ = 255° at advance ratio of 0.35. Another notable point seen in the comparison of the lift coefficient is related to the maximum value of this coefficient, which is formed in relation to the DSV strength, so that at advance ratio of 0.3, the maximum value of the lift coefficient is created at $\psi$ = 270 degrees (the end of the third quadrant), which is the pitch-up motion of the blade. However, at advance ratio of 0.35, the maximum lift coefficient occurs at $\psi$ = 295 degrees in the fourth quadrant, where the rotor blade has a pitch-down motion. It is predicted that with increasing advance ratio, despite the larger pitch angle and greater flow separation at the same position (equal azimuth angle), due to the higher tangential velocity, the amount of shear stress at the leading edge also increases, which will cause more energy injection from vortices generation into the boundary layer and greater resistance to the separation of the DSV, thus the maximum lift coefficient occurred at a higher azimuth angle in flight with advance ratio of 0.35. In fact, the strengthening of the boundary layer at a high pitch angle causes stall delay, although the flow motion along the blade span also plays an important role in the stability and persistence of the DSV in the rotor blade radial sections [19]. In summary, the effect of increasing the advance ratio on the dynamic stall of the radial section with *r/R* = 0.778 was studied. The results show that at $\mu$ = 0.3, there were multiple dynamic stalls in the retreating side of the rotor, while only one substantial stall occurred at $\mu$ = 0.35. However, high advance ratio caused shock-induced stall on the rotor blade's advancing side, which was more critical. The following briefly examines the effects of dynamic stall limitations on aerodynamic damping and the possibility of stall flutter.

Stall flutter is a single-degree-of-freedom instability seen in helicopter blades and turbomachinery. It occurs when the combination of aerodynamic and structural damping becomes negative, increasing the amplitude of the structure's vibration response. Negative values of aerodynamic damping indicate increased instability and cause radial sections to be vulnerable to stall flutter. The average aerodynamic damping value per cycle for the pitching radial section is calculated using the equation below [20].

$$\Xi_{cycle} = -CW/(\pi {\alpha_1}^2) = -\frac{1}{\pi {\alpha_1}^2}\oint C_m d\alpha \qquad (3)$$

In the above equation, *CW* is represents the energy transferred between the airflow and the cross section, $C_m$ is the pitching moment coefficient around the aerodynamic center, and $\alpha_1$ is the pitching amplitude of the radial cross section. Table 2 shows the average values of this coefficient in the studied cross section for two advance ratios.

**Table2. Average aerodynamic damping coefficient**

| $\mu$ | $\Xi_{cycle}$ |
|---|---|
| 0.3 | -0.0015 |
| 0.35 | -0.0403 |

Table 2 indicates that at $\mu$=0.35, the average aerodynamic damping value is significantly larger than at $\mu$=0.3, indicating increased vibrations at higher flight speeds. This large discrepancy shows a greater sensitivity to stall flutter at high advance ratio than at moderate advance ratio.

## 5. Conclusion

In this study, the effect of the advance ratios ($\mu$ = 0.3 and $\mu$ = 0.35) on the dynamic stall in the outboard region of the rotor blade with a pitching motion has been investigated using numerical simulation. The key findings of this study include the following:

1- At both advance ratios, the flow field under study was highly complex and unsteady. It showed trailing edge separation, shear layer roll-up, vortex evolution, dynamic stall vortex, and shock-induced separation at most rotor azimuth angles.
2- By comparing the aerodynamic loads at the studied at $r/R$ = 0.778, it was found that the major limitation due to stall $\mu$ = 0.35 was in the advancing side of the rotor. However, $\mu$ = 0.3, the comparison of the coefficients indicates that more and more severe stalls occur in the retreating side of the rotor.
3- Average aerodynamic damping values indicate that the probability of stall flutter is higher at $\mu$ = 0.35 than $\mu$ = 0.3.
4- The mechanism of stall occurrence in the advancing side of the rotor at both advance ratios is related to compressibility and shock wave formation near the leading edge. In the retreating side, stall development at both advance ratios is due to the spread of trailing edge separation and roll-up of the shear layer and the formation of a turbulence separation vortex.
5- The pressure distribution on the blade surface shows a larger low-pressure region at the leading edge of the blade at $\mu$ = 0.3. This phenomenon is directly related to the spread of the trailing edge separation, which at $\mu$ = 0.35 extends to the vicinity of the leading edge and reduces the maximum suction in this region, while at $\mu$ = 0.3 it extends to the maximum airfoil thickness.
6- Examination of the shear stress lines at both advance ratios in the phase of increasing blade pitch angle reveals the formation of stall cells, which imply the presence of an omega vortex lift-off from the blade surface.

## 6. Refrences


[1] McCroskey WJ, Carr LW, McAlister KW (1976) Dynamic stall experiments on oscillating airfoils. *AIAA Journal*, 14(1), 57-63.

[2] Carr LW, McAlister KW, McCroskey WJ (1977) *Analysis of the development of dynamic stall based on oscillating airfoil experiments* (In NASA technical note).

[3] McCroskey WJ (1981) *The phenomenon of dynamic stall* (In NASA technical note).

[4] Carr LW, Chandrasekhara MS (1996) Compressibility effects on dynamic stall. *Progress in Aerospace Sciences*, 32(6), 523-573.

[5] Gharali K, Johnson DA (2013) Dynamic stall simulation of a pitching airfoil under unsteady freestream velocity. *Journal of Fluids and Structures*, 42, 228-244.

[6] Benton SI, Visbal MR (2019) The onset of dynamic stall at a high, transitional Reynolds number. *Journal of Fluid Mechanics*, 861, 860-885.

[7] Coton FN, Galbraith, RM (1999) An experimental study of dynamic stall on a finite wing. *The Aeronautical Journal*, 103(1023), 229-236.

[8] Le Pape A, Pailhas G, David F, Deluc J M (2007) Extensive wind tunnel tests measurements of dynamic stall phenomenon for the OA209 airfoil including 3D effects.

[9] Spentzos A, Barakos G, Badcock K, Richards B, Wernert P, Schreck S, Raffel M (2005) Investigation of three-dimensional dynamic stall using computational fluid dynamics. *AIAA journal*, 43(5), 1023-1033.

[10] Spentzos A, Barakos GN, Badcock KJ, Richards BE, Coton FN, Galbraith RM, Favier D (2007) Computational fluid dynamics study of three-dimensional dynamic stall of various planform shapes. *Journal of Aircraft*, 44(4), 1118-1128.

[11] Letzgus J, Keßler M, Krämer E (2020) Simulation of dynamic stall on an elastic rotor in high-speed turn flight. *Journal of the American Helicopter Society*, 65(2), 1-12.

[12] Esfahani FH, Karimian SM H (2024) Three-Dimensional Numerical Investigation on the Dynamic Stall Behavior of the Helicopter Rotor Blade at Forward Flight Speeds. *Arabian Journal for Science and Engineering*, 1-21.

[13] Leishman, G. J. (2006). Principles of helicopter aerodynamics. *Cambridge university press*.

[14] Roe PL (1986) Characteristic-based schemes for the Euler equations. *Annual review of fluid mechanics*, 18(1), 337-365.

[15] Blazek J (2015) Computational fluid dynamics: principles and applications. *Butterworth-Heinemann*.

[16] Fluent, ANSYS (2019) Ansys fluent theory guide. *Ansys Inc*., USA, 15317, 724-746.

[17] Tejero EF, Doerffer P, Szulc O (2016) Application of a passive flow control device on helicopter rotor blades. *Journal of the American helicopter society*, 61(1), 1-13.

[18] Corke TC, Thomas, FO (2015) Dynamic stall in pitching airfoils: aerodynamic damping and compressibility effects. *Annual Review of Fluid Mechanics*, 47(1), 479-505.

[19] Raghav V, Komerath N (2015) Advance ratio effects on the flow structure and unsteadiness of the dynamic-stall vortex of a rotating blade in steady forward flight. *Physics of Fluids*, 27(2).

[20] Bowles PO, Corke TC, Coleman DG, Thomas FO, Wasikowski M (2014) Improved understanding of aerodynamic damping through the Hilbert transform. *AIAA Journal*, 52(11), 2384-239